Ceramics International 44 (2018) 12655–12663

Contents lists available at ScienceDirect

Ceramics International

journal homepage: www.elsevier.com/locate/ceramint

Transient thermal stress due to the penetration of calcium-magnesium-alumino-silicate in EB-PVD thermal barrier coating system

Guanghui Zhang[a], Xueling Fan[a,*], Rong Xu[a], Luochuan Su[b], T.J. Wang[a]

[a] State Key Laboratory for Strength and Vibration of Mechanical Structures, School of Aerospace Engineering, Xi'an Jiaotong University, Xi'an 710049, China
[b] Institute of Fluid Physics, China Academy of Engineering Physics, Mianyang 621999, China

ARTICLE INFO

Keywords:
Thermal barrier coating (TBC)
CMAS
Transient thermal stress
Crack

ABSTRACT

Electron beam-physical vapor deposited (EB-PVD) thermal barrier coating system (TBCs) are vulnerable to the degradations induced by the penetration of calcium- magnesium-alumino-silicate (CMAS). In this work, we conduct a numerical study to investigate the effect of CMAS penetration on the development of transient thermal stress in EB-PVD TBCs with the columnar microstructure. A two-dimensional periodical model is developed, taking into account the columnar microstructure of EB-PVD TBCs and the CMAS penetration. We found that the CMAS penetration would induce a field of high in-plane tensile stress in TC upon the rapid cooling, promoting the initiation of the vertical cracks from top surface toward to the bottom of TC. Meanwhile, the accumulation of out-of-plane tensile stress tends to occur at the side edges of EB-PVD columns near three main regions: closely beneath the top surface of TC, at the interface between CMAS penetrated and non-penetrated zone, and close to the TC/BC interface. Therefore, the horizontal cracks are likely to initiate from the side edges of EB-PVD columns at these three regions, which agrees well with experiments.

1. Introduction

Thermal barrier coating system (TBCs) is essential for the thermal protection of gas turbine engines. Typical TBCs consist of four primary constituents [1–4]: the ceramic top-coat (TC) providing the thermal insulation, thermally grown oxide (TGO) formed upon the high temperature oxidation, the superalloy substrate (Sub) and the bond-coat (BC) sprayed between the TC and Sub to against the substrate oxidation and reduce the thermal expansion mismatch. There are two main types of methods to fabricate TBCs: air plasma spray (APS) and electron beam-physical vapor deposition (EB-PVD) [1,5,6]. The EB-PVD coating generates a column grain structure with multiscale porosity while the APS coating exhibits a layered architecture.

Serving under high temperature environment, TBCs is subjected to various degradation mechanisms such as sintering [7,8], oxidation [9,10], hot corrosion [11,12], and thermal expansion mismatch [13–15]. With the special column structure as shown in Fig. 1(a), EB-PVD TBCs would exhibit the excellent durability in service. The inner space between the columns of EB-PVD coating contributes to improve the strain tolerance as well as reduces the thermal conductivity [5,16,17]. Nevertheless, with the elevated turbine inlet temperature and under extreme service conditions, EB-PVD TBCs is susceptible to the degradations induced by the molten deposits, that is, a combination of impurities brought in with the fuel and/or the air. The constituents of the deposits are glass-forming oxides of calcium, magnesium, aluminum and silicon (CMAS)[18–22]. CMAS adheres to the surface of TBCs and it would be molten when the surface temperature exceeds its melting point (typically 1250 °C) [23–25]. Subsequently, owing to the remarkable wetting ability and low viscosity, molten CMAS would easily penetrate into the inner space between the columns of EB-PVD coating by capillarity action. Ultimately, the penetrated molten CMAS would solidify and occupy the inner space between the columns of EB-PVD coating upon the cooling stage such as the regular shutdowns of gas turbine, leading to a significant deterioration of the strain tolerance and thermal insulation performance. Under this circumstance, large thermal stresses developed from the thermal expansion mismatch between layers would trigger the formation of surface crack, interfacial delamination, and final spallation of the ceramic coating (Fig. 1(b)) [24,26–32].

The degradation mechanisms caused by CMAS penetration have been intensively studied. Stott et al.[22], Smialek et al.[18,19] and Kim et al.[21] explored the environmental deposition and erosion of the hot sections such as combustors and vanes in turbines, respectively. It was observed that sand particles, composed of calcium-aluminum silicates, deposited on the hot sections and resulted in the deterioration of mechanical and thermal performance. By inspecting the airfoil removed

* Corresponding author.
E-mail address: fanxueling@mail.xjtu.edu.cn (X. Fan).

https://doi.org/10.1016/j.ceramint.2018.04.065
Received 14 March 2018; Received in revised form 8 April 2018; Accepted 9 April 2018
Available online 10 April 2018

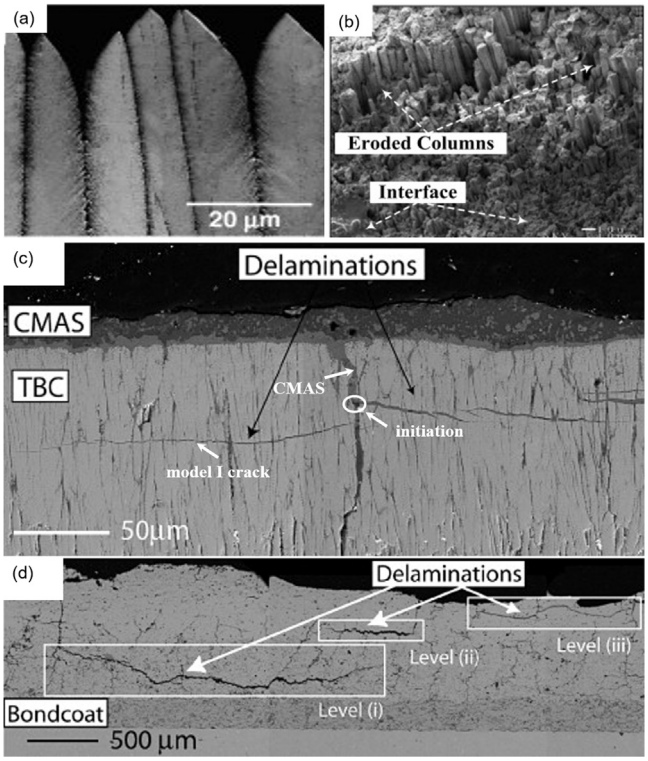

Fig. 1. Scanning electron micrographs of EB-PVD thermal barrier coatings: (a) The columnar microstructure of ceramic top-coat [33]; and (b) A TBC sample with the spallation of top-coat after CMAS penetration. Some columns are completely removed and the inner interface is exposed to environment [27]. (c) Delamination induced by the penetration of CMAS reported in Mercer's work [26]; (d) Delamination at three different levels in the CMAS-penetrated hot-section aero-turbine components reported by Krämer et al. [23].

during service, Mercer et al. [26] identified three typical features associated with the CMAS induced spalling, as shown in Fig. 1(c): (I) The sub-surface delamination always initiates at the surface-connected vertical separations. (II) The delamination is fully penetrated by CMAS. (III) The fracture mode of the delamination is strictly restricted to model I. Krämer et al. [28] found that multiple sub-surface delaminations were evident in the hot-section of aero-turbine components subjected to the CMAS penetration. The delamination was located at three primary levels, as shown in Fig. 1(d): (i) closely above the bond coat, (ii) adjacent to the bottom of the CMAS-penetrated layer and (iii) closely beneath the top surface. They established a framework to explain the experimental observations through mechanistic analyzing the evolution of the thermo-elastic stresses upon cooling and associated channel-crack propagation and interfacial delamination. More recently, Su et al.[34] developed a model incorporating the CMAS penetration into the EB-PVD coating with the columnar microstructure. The theoretical and numerical analysis indicates that CMAS penetration primarily affects the overall in-plane modulus of TC layer that plays a key role on the energy release rate and mode mixity of the interfacial delamination.

However, the majority of the previous work focuses on the stress evolution and failure formulation within TBCs under CMAS penetration after cooling. Transient thermal gradient caused by abrupt cooling, acting as a significant role on the evolution of stresses, has been rarely taken into account in analysis. A comprehensive study [35] illustrated that CMAS penetration assisted cracking and delamination would be triggered by the high thermal mismatch stress which is mainly generated by the higher thermal gradients during the cooling stage. Furthermore, the studies [36,37] demonstrated that stresses generated by transient thermal gradient are more deleterious than those associated

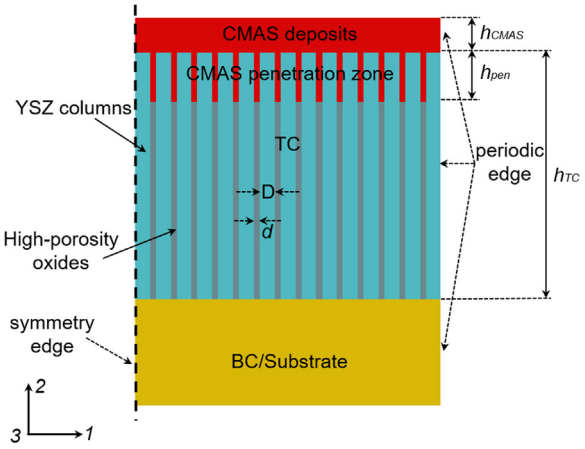

Fig. 2. The schematic view of the finite element model incorporating the column microstructure of EB-PVD TBCs.

with the quasi-steady temperature field upon the slow cooling. Hence, transient thermal gradient plays a critical role on the degradations of TBCs subjected to CMAS penetration upon the cooling process.

In this work, we investigate the effects of CMAS penetration on the transient development of thermal stress in EB-PVD TBCs upon the rapid cooling. In Section 2, the numerical model is developed, and the sequentially coupled thermal-stress simulation method is described. In Section 3, the effects of CMAS penetration on stress development in TC are presented and the failure in the EB-PVD TBCs with CMAS penetration are discussed. Conclusions are drawn in Section 4.

2. Simulation scheme

According to the experimental observations of the microstructure of EB-PVD coating in Fig. 1(a), the plain-strain model of the TBCs incorporating the columnar microstructure is employed, as shown in Fig. 2, where h_{TC} is the thickness of the TC of TBCs, h_{CMAS} is the thickness of CMAS deposited on the surface of TBCs, and h_{pen} is the depth of CMAS penetration zone induced by the penetration of CMAS into the column gaps of EB-PVD coating. The columns of EB-PVD coating are assumed to be initially straight and parallel. The present numerical model includes 200 columns whose width is D and gap in-between is d. The column width of EB-PVD TBCs is taken to be $D = 9\,\mu m$, and the gap is $d = 1\,\mu m$. As a result, the porosity of TC is 10%, a typical value observed in most TBCs [38–40]. Initially, the gaps are filled with highly porous oxides, presenting the as-sprayed TBCs [1]. Followed by the CMAS deposition and penetration, the gaps are gradually filled with CMAS deposits. The thicknesses of BC and substrate, not represented in detail in Fig. 2, are h_{BC} and h_{Sub}, respectively. A typical set of the thickness of each layers $h_{TC} = h_{BC} = 100\,\mu m$ [1,27], $h_{CMAS} = 20\,\mu m$ [26] are selected. The depth of CMAS penetration zone h_{pen} is initially selected as 50 μm and then varies from 0 to 100 μm to investigate the effect of CMAS penetration depth on the stress evolution and failure formation. It should be noted that the interface between the BC and TC is relatively flat for EB-PVD TBCs and thus the TGO layer is smooth without significant undulation [2]. Therefore, for simplification, TGO is ignored in the work.

To simulate the high thermal mismatch stress within the CMAS penetrated TBCs upon rapid cooling, the method of sequentially coupled thermal-stress analysis is employed. We first calculate the transient temperature field during the rapid cooling by finite element method. Then, the temperature filed, which is assumed to be independent on the stress field, was imported as a predefined field into the numerical model to solve the thermal stress field. Finite element analysis was performed by using the commercial code ABAQUS 6. 14 [41]. The models were meshed by around 2243000 four-node quadrilateral elements (DC2D4

Table 1
The material properties of TBCs, CMAS and highly porous oxides filled in gaps [27,43–47].

Layer	E(GPa)	ν	ρ(kg/m^3)	K($Wm^{-1}K^{-1}$)	$\alpha\times10^{-6}(°C^{-1})$	$c\times10^{-6}$ ($Jkg^{-1}K^{-1}$)
TC	40	0.2	5650	1.05	11	483
BC	180	0.3	7320	6.4	16	592
Substrate	200	0.3	8220	17.3	14	524
CMAS	84	0.25	2540	1.78	8.1	875
High porosity oxides	2	0.25	1000	0.2	11	483

in thermal analysis and CPE4R in stress analysis). The meshes in TC are refined for improving the accuracy and reliability. The mesh sensitivity study has been performed and indicates that the mesh refinement is sufficient to achieve mesh size independent results.

The TBCs used in this work is composed of an Inconel 617 substrate, a NiCoCrAlY BC and a yttria partially stabilized zirconia (ZrO_2–8 wt% Y_2O_3) TC. All layers of TBCs in the finite element model are assumed to be homogeneous and isotropic [42]. To obtain a qualitative insight into the behavior of TBCs, the TC, BC and substrate are treated as linear elastic materials. The typical mechanical and thermal properties of TBCs are listed in Table 1 [27,43–45]. During cooling stage, the temperature in TC is always below the melting point of CMAS (~1250 °C). Therefore, it is reasonable to treat the CMAS as a crystallized material whose material properties are also listed in Table 1 [46,47]. The hypothetical mechanical and thermal properties of highly porous oxides are also listed in Table 1. It should be noted that the selected values for highly porous oxides might not represent their real material property. Nevertheless, we can still get a qualitative insight because the highly porous oxides have negligible effect on the stress evolution owing to their small volume fraction in the TC.

Two kinds of boundary conditions, mechanical and thermal boundary conditions, are employed in the sequentially coupled thermal-stress analysis to solve the temperature and stress fields. The finite element model in this work is assumed as a representative unit of an overall TBCs. Periodic mechanical boundary condition is employed in simulation, as shown in Fig. 2, where the symmetry boundary condition is imposed on the left side and the right side is allowed to move but the horizontal displacements of all the nodes on the right side are restricted to be consistent [42]. Thermal history representing the cooling process has two stages, as shown in Fig. 3. It is assumed that before rapid cooling the TBCs has been in service within the high temperature for a long time. Therefore, at t = 0 s, the temperature of the surface of CMAS deposits is specified as $T_{sur}(0) = 1425$ °C, and the temperature of the bottom of substrate is set as $T_{bottom}(0) = 870$ °C. The consequent temperature gradient in TBCs as schematically shown in Fig. 3(a) represents the temperature distribution for the initial "hot" state. The stresses within TBCs are assumed to be zero in the initial "hot" state owing to the fact that the creep is expected to relax stresses at high temperatures. For t > 0 s, rapid cooling is simulated by abruptly imposing a cooling gas flow with $T_{gas}(0) = 25$ °C on the surface of CMAS. The heat transfer coefficient of CMAS surface $H_{sur} = 1500 Wm^{-2}K^{-1}$ represents the forced air cooling, while the heat transfer coefficient of substrate bottom $H_{bottom} = 200 Wm^{-2}K^{-1}$ represents radiative cooling and nature convection [36]. The total cooling time is set as 100 s to ensure the TBCs completely cooled down. Transient thermal effect is taken into account in the process of cooling.

3. Results and discussions

According to the thermal history shown in Fig. 3, the transient temperature field in the TBCs during rapid cooling are plotted in Fig. 4 where the x-axis represents the distance to the top surface of TC. The initial temperature gradient between the surface of TC and the interface between TC and BC is 175 °C at t = 0 s. The average temperature in TC is 1312.5 °C, higher than the melting point of CMAS (~1250 °C). Therefore, the penetrated CMAS is in a molten state. However, once the cooling process started, the temperature of TC immediately dropped below the melting point of CMAS, leading to the crystallization of CMAS. Consequently, it is reasonable to treat CMAS as a crystallization material in the whole cooling process. The temperature at the surface of TC drops about 600 °C within 0.5 s after the start of the cooling process while the temperatures in the BC and substrate change little relatively, as shown in Fig. 4. This dramatic temperature decrease of the TC during the rapid cooling generates a field of high tensile stress and associated high energy release rate for the delamination in TC. In addition, it is worth noting that the temperature of the bottom of substrate is slightly increased until 0.5 s, as shown in Fig. 4. The slight temperature increase at the bottom is owing to the homogenization of the temperature distribution within the substrate. In specific, the high temperature difference between the TC surface and substrate is removed during the cooling, the temperature distribution within substrate tends to be homogenized as no temperature difference could further support this

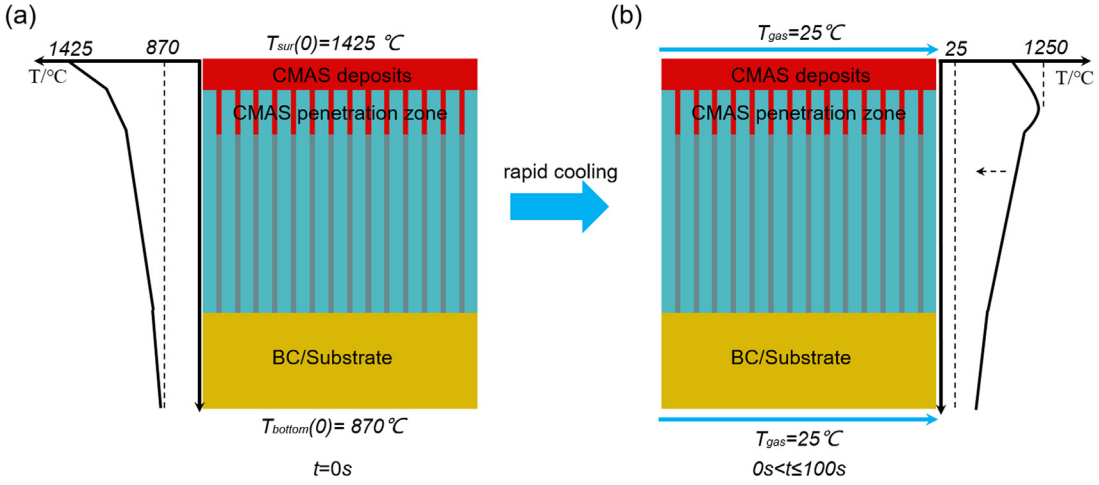

Fig. 3. Thermal boundary conditions of the finite element model (a) before and (b) during the cooling.

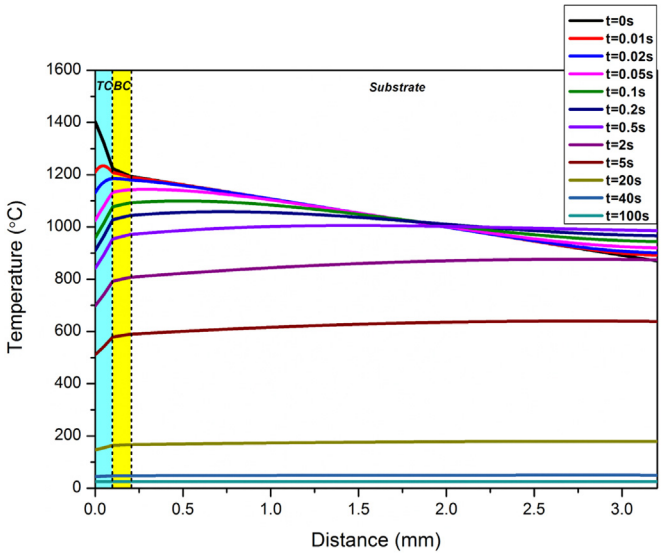

Fig. 4. Transient temperature distributions in the TBCs with the CMAS penetration depth h_{pen} = 50 μm.

temperature gradient. Note that the thermal conduct conductivity of the substrate ($17.3 Wm^{-1}K^{-1}$.) is higher than the heat transfer between the cooling air and the substrate (200 $Wm^{-2}K^{-1}$), thus, the homogenization would dominate the initial cooling stage until the temperature distribution in the substrate becomes homogeneous at 0.5 s. Then the temperature of the whole substrate gradually decreases due to the convection heat transfer by cooling gas. Imposed by the cooling gas with the temperature of 25 °C, the temperature of TBCs reached 25 °C after the cooling for 100 s, as shown in Fig. 4.

3.1. The evolution of stress in TC

To analyze the evolution of the stress in CMAS penetrated TBCs upon the rapid cooling, we plot the contours of the in-plane and out-of-plane stresses σ_{11} and σ_{22} within TC at different cooling time, as shown in Fig. 5(a) and (b). For the in-plane stress contours in Fig. 5(a), σ_{11} in TC is tensile initially and gradually becomes compressive accompanied with the cooling. In Fig. 5(b), σ_{22} in CMAS penetrated zone gradually increases while σ_{22} in CMAS non-penetrated zone almost maintains zero in the whole cooling process. Three regions with distinct σ_{22} concentration could be easily observed in Fig. 5(b): upper region located just beneath the top surface of TC, middle region at the interface between CMAS penetration and non-penetration zones, and lower region close to the TC/BC interface, respectively.

As shown in Fig. 5(a) and (b), the stress distribution within the single column of TC exhibits a significant difference with that close to the gaps between two columns. Hence, two representative paths as shown in Fig. 6(a) are chosen to help analyze the evolution of the stress in TC. One path, *path_r*, is along the side edge of the column and another path, *path_z*, is assigned in the middle of the column. Fig. 6(b-e) plots the distributions of in-plane stress σ_{11} and out-of-plane stress σ_{22} along two different paths in TC. The distribution of σ_{11} along the two paths in TC at different cooling time are plotted in Fig. 6(b) and (c). For *path_r* and *path_z*, σ_{11} in TC always increases substantially upon the initial cooling such as $t < 0.5$ s, then gradually decrease, and finally becomes compressive. σ_{11} in CMAS penetrated zone during cooling process varies more dramatically than that in CMAS non-penetrated zone. It indicates that CMAS penetration plays a critical role on the stress evolution in TC. In addition, along *path_r*, a peak of stress distribution appears at the interface between CMAS penetrated and non-penetrated zone, as shown in Fig. 6(c). However, no oscillation of stress distribution is observed at the same location along *path_z*, where σ_{11} exhibits a continuous drop from high tensile level to the low one.

The distributions of σ_{22} in TC along two paths at different cooling time are plotted in Fig. 6(d) and (e). For both paths, σ_{22} in CMAS penetrated zone gradually accumulates such that σ_{22} reaches the maximum value at the end of cooling process. However, in CMAS non-penetrated zone, σ_{22} remains a low level around zero upon the whole cooling process. Along *path_r*, it is obvious that the cooling process would generate three peaks in σ_{22} distributions that are located beneath

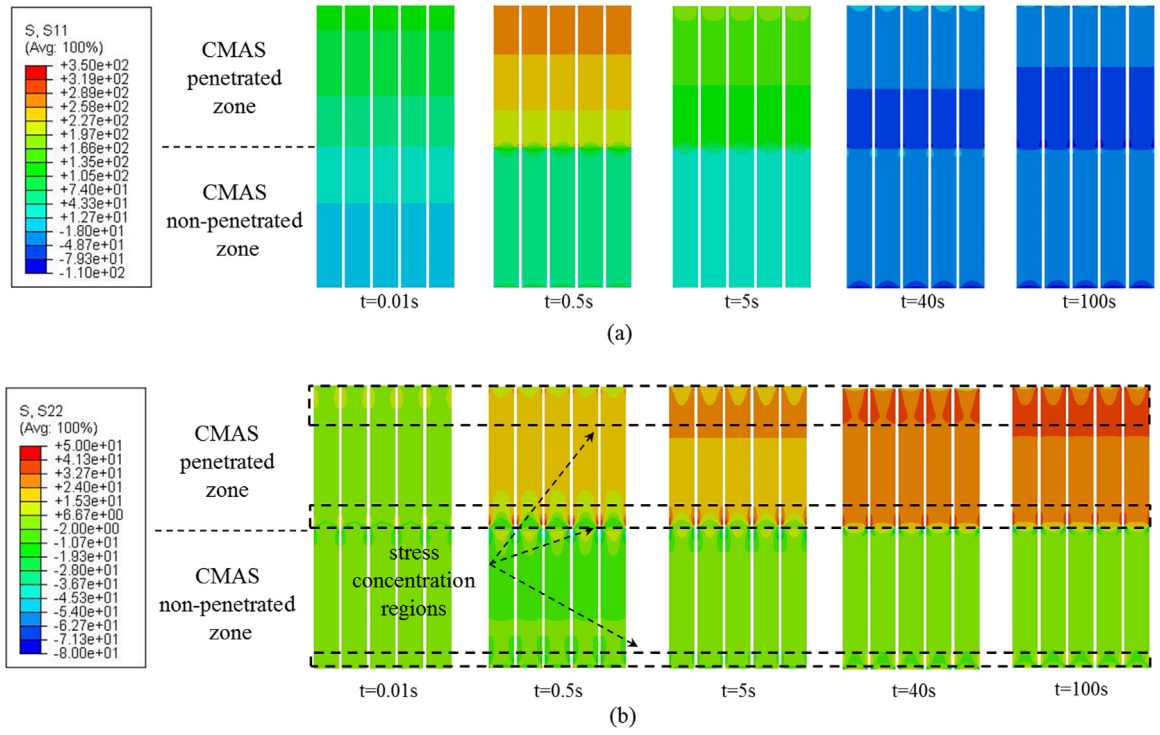

Fig. 5. Contours of (a)σ_{11}(MPa) and (b)σ_{22}(MPa) in the TC at different cooling time.

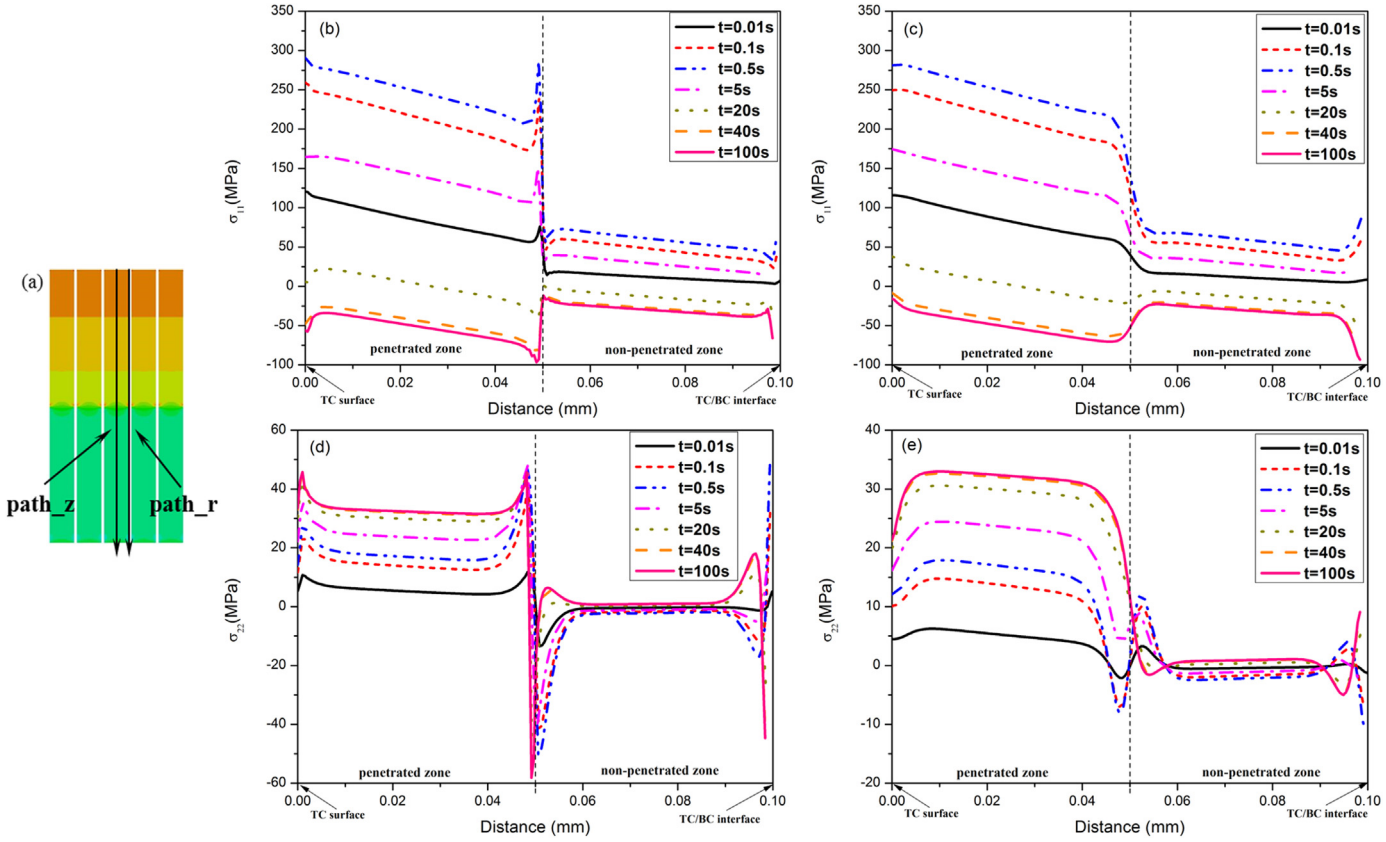

Fig. 6. (a) Two paths in TC, path_r and path_z, are selected for the stress analysis in CMAS penetrated TBCs upon cooling. Distributions of in-plane stress σ_{11} (MPa) along (b) path_r and (c) path_z. Distributions of out-of-plane stress σ_{22} (MPa) along (d) path_r and (e) path_z.

the top surface of TC, at the interface between CMAS penetrated and non-penetrated zone and close to the TC/BC interface, respectively, as shown in Fig. 6(d). Compared with the distributions of σ_{22} along *path_z* in Fig. 6(e), these oscillations of σ_{22} in Fig. 6(d) would induce several regions with much higher stress, which promotes the formation of horizontal cracks at these locations of the column side edge and then propagating to the middle of the column.

3.2. The effect of CMAS penetration on the stress distribution in TC

The depth of CMAS penetration depends on the temperature distributions in TC before cooling [43]. During service, the temperature distributions are not uniform in TC due to the complex microstructure such that CMAS penetrates into TC with different depths. In the numerical model, the depth of CMAS penetration is assumed to vary from 0μm to 100μm (h_{pen} = *0, 25, 50, 75, 100* μm) to investigate the effect of CMAS penetration depth on the stress in TC. Three representative points in TC, with distances of 25μm, 50μm and 75μm to the top surface of TC, are selected herein. The stress states at these points are used to investigate the effect of CMAS penetration depth on the stress in TC, as shown in Fig. 7(a–i). For the point that is 25μm beneath TC surface, the magnitudes of σ_{11} and σ_{22} are relatively small without CMAS penetration (h_{pen} = *0* μm), as shown as the black curves in Fig. 7(b) and (c). For the shallow CMAS penetration into TC (h_{pen} = *25* μm), the peak values of σ_{11} and σ_{22} increase significantly, as shown as the red curves in Fig. 7(b) and (c). Once CMAS deposits penetrates over this representative point (h_{pen} = *50* μm), the peak value of σ_{11} would slightly increases while σ_{22} still shows an apparently increase. However, the continuous CMAS penetration has little influence on the stress of this representative point once CMAS deposits has penetrated over it, which could be easily confirmed by the coincidence of the curves of σ_{11} and σ_{22} for CMAS penetration depth over 25μm (i.e. h_{pen} = 50μm, 75μm and 100μm), as shown in Fig. 7(b) and (c). However, the amplifications for the dotted boxes indicate that the continuous CMAS penetration induces the decrease of the stresses at this point despite it is really small, as shown as the insert figures. The similar conclusions can be obtained for the representative points with the depths of 50μm and 75μm to the top surface. In addition, the black, red and blue curves in Fig. 7(h) and (i) are coincident, which suggests that CMAS has little effect on the stress at the point that CMAS has not penetrated over it. Therefore, the stress in CMAS penetrated TC can be classified into three types: Type I, for the regions far from CMAS penetration, stresses are relatively small and the continuous penetration of CMAS has no effect on the stress filed. Type II, for the regions where CMAS penetration just reaches, the stresses increase remarkably. Type III, for the regions already covered by CMAS penetration, the stresses increase again and continuous CMAS penetration will slightly mediate the stresses.

The effects of CMAS penetration on the stress distributions along the TC thickness are presented in Fig. 8. The same paths shown in Fig. 6(a) are selected to represent the stress distributions in TC. The distributions of σ_{11} in TC along two paths at cooling time t = 0.5 s are plotted in Fig. 8(a) and (c). Cooling time t = 0.5 s is particularly selected because at this moment σ_{11} reaches the maximum value, as shown in Fig. 7(b), (e) and (h), indicating the high possibility of the formation of surface-connected vertical separations. Similarly, σ_{22} in TC along two paths at 100 s are selected and plotted in Fig. 8(b) and (d). For the cases in Fig. 8, the black curves always represent the stress in TC without CMAS penetration from which we observe that σ_{11} and σ_{22} are relatively small. However, with the initial CMAS penetration, the stresses would significantly increase. The continuous CMAS penetration seems to have a little influence on the stress in TC because the insert figures of Fig. 8(a)–(b) show that the continuous CMAS penetration would slightly reduce σ_{11} along two paths. Similarly, the effect of CMAS penetration on σ_{22} is presented in Fig. 8(b) and (d). The peak values of σ_{22}

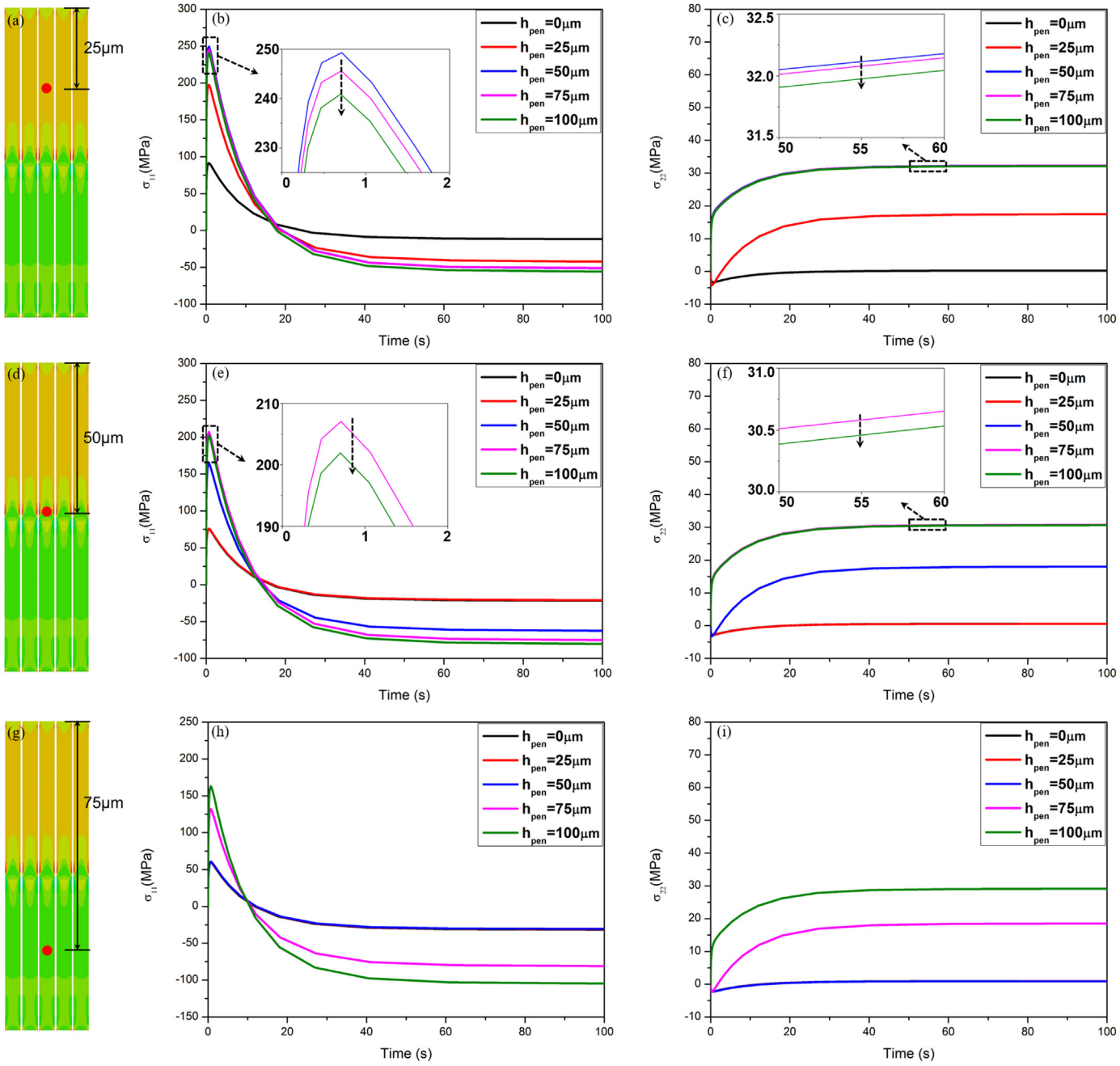

Fig. 7. Stress evolutions at three depths in the TC for different CMAS penetration depths. The points with the depths of (a)25 μm, (d)50 μm and (g)75 μm to the top surface. (b) in-plane stress σ_{11} (MPa) and (c) out-of-plane stress σ_{22} (MPa) evolution of the point with the depth of 25 μm to the top surface. (e) in-plane stress σ_{11} and (f) out-of-plane stress σ_{22} evolution of the point with the depth of 50 μm to the top surface. (h) in-plane stress σ_{11} and (i) out-of-plane stress σ_{22} evolution of the point with the depth of 75 μm to the top surface.

at the interface between CMAS penetrated non-penetrated zone along *path_r* tend to decrease with the continuous CMAS penetration, as showed in Fig. 8(c). This decrease of the maximum σ_{22} in TC is attributed to the continuous filling of CMAS deposits into the gaps between columns. Under this circumstance, the solidified CMAS deposits in the gaps would compensate the thermal mismatch strain between TC and substrate upon the cooling, and thus mediate the thermal mismatch stress within TC.

3.3. CMAS penetration induced failure

The CMAS penetration would induce much higher in-plane tensile stress in TC upon the rapid cooling, promoting the initiation of vertical cracks from top surface toward to the bottom of TC. Meanwhile, the accumulation of out-of-plane tensile stress tends to occur at the side edges of EB-PVD columns near three main regions: closely beneath the top surface of TC, at the interface between CMAS penetrated and non-penetrated zone, and close to the TC/BC interface. Therefore, the horizontal cracks are likely to initiate from the side edges of EB-PVD columns at these three regions, which is in good agreement with the experimental observations by Krämer et al. [23]. Based on the stress analysis, a schematic predicating the crack formations in EB-PVD TBCs with CMAS penetration are shown in Fig. 9. At the initial cooling, the vertical crack forms from TC surface and the horizontal delamination initiates from the side edges of columns at three regions where out-of-plane tensile stress accumulates. With the continuous propagation of

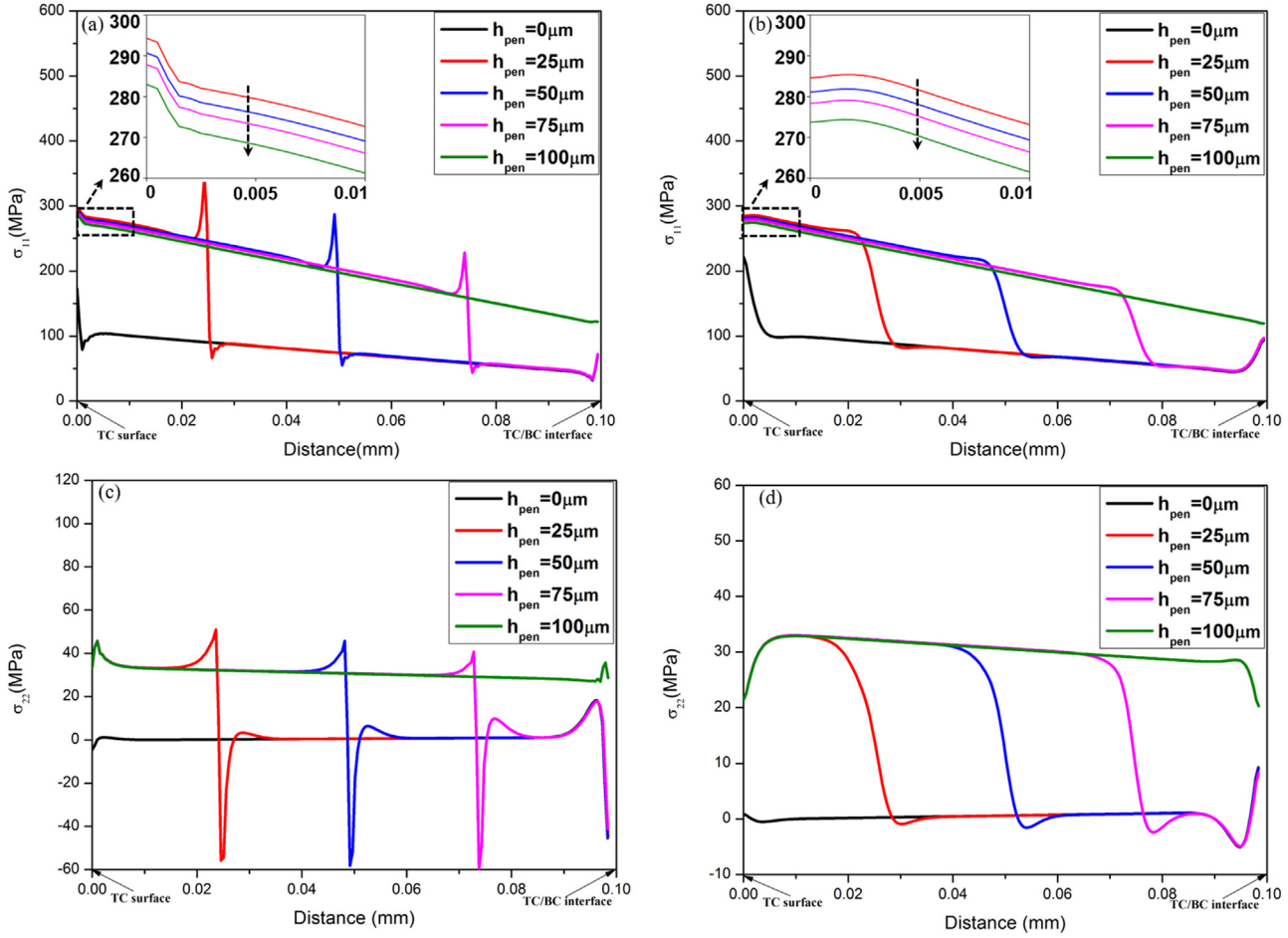

Fig. 8. Distributions of σ_{11} and σ_{22} in TC along two paths for different depths of CMAS penetration. (a) σ_{11} (MPa) along path_r at 0.5 s, (b) σ_{11} along path_z at 0.5 s, (c) σ_{22} (MPa) along path_r at 100 s, (d) σ_{22} along path_z at 100 s.

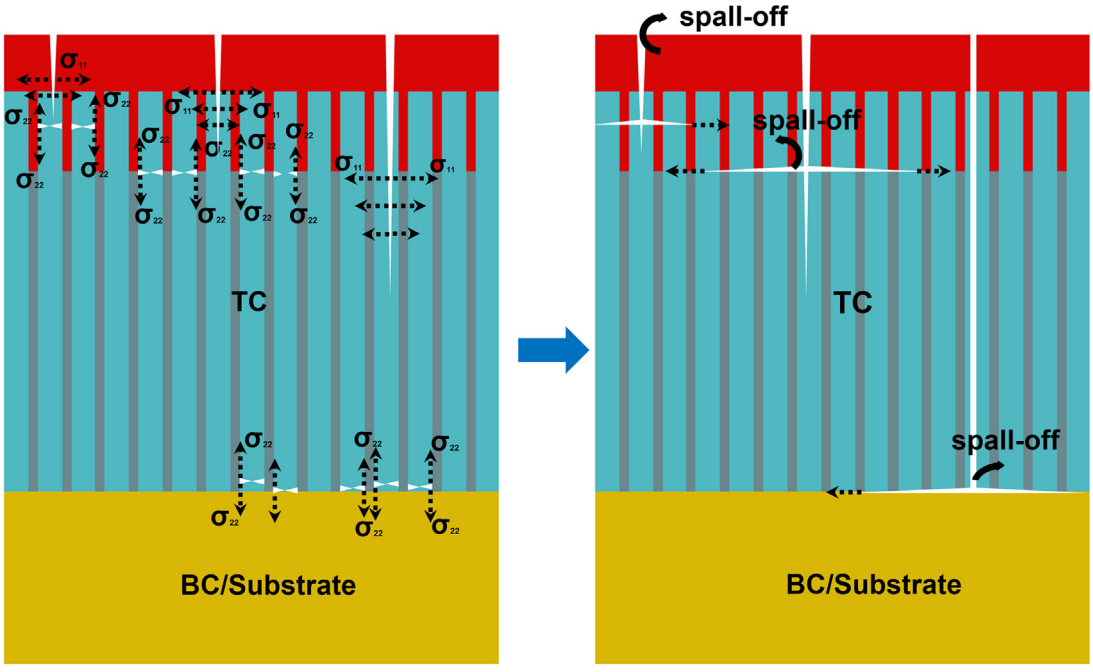

Fig. 9. Schematic showing the cracking modes in EB-PVD TBCs with CMAS penetration.

cracks upon the cooling, horizontal cracks coalesce each other or with the vertical cracks to induce large scale spalling of TC from the substrate, leading to the ultimate failure of TBCs.

4. Conclusions

This work presents the numerical analysis of the transient thermal stress in CMAS penetrated TBCs upon cooling. A representative two-dimensional periodical model is developed, taking into account the columnar microstructure of EB-PVD TBCs and CMAS penetration. The role of CMAS penetration on the stress field is mechanistically investigated. It is found that large in-plane and out-of-plane tensile stresses will arise within CMAS penetrated zone upon cooling while the stresses in CMAS non-penetrated zone would remain marginal. The field of high in-plane tensile stress in TC upon the rapid cooling will promote the initiation of the vertical cracks from top surface toward to the bottom of TC. Meanwhile, out-of-plane tensile stress accumulates at the side edges of columns around three regions, i.e. beneath the top surface of TC, at the interface between CMAS penetrated and non-penetrated zone, and close to TC/BC interface. Therefore, the horizontal cracks are likely to initiate from the side edges of EB-PVD columns at these three regions. Investigation reveals that the stress in CMAS penetrated TC can be classified into three types: Type I, for the regions far from CMAS penetration, stresses are relatively small and the continuous penetration of CMAS has no effect on the stress filed. Type II, for the regions where CMAS penetration just reaches, the stresses increase remarkably. Type III, for the regions already covered by CMAS penetration, the stresses increase again and continuous CMAS penetration will slightly mediate the stresses. Continuous CMAS penetration slightly reducing the stresses in CMAS penetrated zone is because that the solidified CMAS deposits in the gaps would compensate the thermal mismatch strain between TC and substrate upon cooling, and thus mediate the thermal mismatch stress within TC. This study provides a mechanistic understanding of the failure mechanisms in CMAS penetrated EB-PVD TBCs upon cooling, which might be truly rewarding in the development of EB-PVD TBCs.

Acknowledgement

This work was supported by NSFC (11472204, 11602188, 11602246).

References

[1] A.G. Evans, D.R. Mumm, J.W. Hutchinson, G.H. Meier, F.S. Pettit, Mechanisms controlling the durability of thermal barrier coatings, Prog. Mater. Sci. 46 (2001) 505–553.
[2] N.P. Padture, M. Gell, E.H. Jordan, Thermal barrier coatings for gas-turbine engine applications, SCIENCE 296 (2002) 280–284.
[3] D.R. Clarke, M. Oechsner, N.P. Padture, Thermal-barrier coatings for more efficient gas-turbine engines, MRS Bull. 37 (2012) 891–898.
[4] R. Rajendran, Gas turbine coatings – an overview, Eng. Fail. Anal. 26 (2012) 355–369.
[5] S. Sampath, U. Schulz, M.O. Jarligo, S. Kuroda, Processing science of advanced thermal-barrier systems, MRS Bull. 37 (2012) 903–910.
[6] C. Cai, S. Chang, Y. Zhou, L. Yang, G. Zhou, Microstructure characteristics of EB-PVD YSZ thermal barrier coatings corroded by molten volcanic ash, Surf. Coat. Tech. 286 (2016) 49–56.
[7] B. Lv, H. Xie, R. Xu, X. Fan, W. Zhang, T.J. Wang, Effects of sintering and mixed oxide growth on the interface cracking of air-plasma-sprayed thermal barrier coating system at high temperature, Appl. Surf. Sci. 360 (2016) 461–469.
[8] B. Lv, X. Fan, H. Xie, T.J. Wang, Effect of neck formation on the sintering of air-plasma-sprayed thermal barrier coating system, J. Eur. Ceram. Soc. 37 (2017) 811–821.
[9] L. Su, W. Zhang, Y. Sun, T.J. Wang, Effect of TGO creep on top-coat cracking induced by cyclic displacement instability in a thermal barrier coating system, Surf. Coat. Tech. 254 (2014) 410–417.
[10] Y. Sun, J. Li, W. Zhang, T.J. Wang, Local stress evolution in thermal barrier coating system during isothermal growth of irregular oxide layer, Surf. Coat. Tech. 216 (2013) 237–250.
[11] S.Y. Park, J.H. Kim, M.C. Kim, H.S. Song, C.G. Park, Microscopic observation of degradation behavior in yttria and ceria stabilized zirconia thermal barrier coatings under hot corrosion, Surf. Coat. Tech. 190 (2005) 357–365.
[12] M.R. Loghman-Estarki, R.S. Razavi, H. Edris, S.R. Bakhshi, M. Nejati, Comparison of hot corrosion behavior of nanostructured ScYSZ and YSZ thermal barrier coatings, Ceram. Int. 42 (2016) 7432–7439.
[13] M. Martena, D. Botto, P. Fino, S. Sabbadini, M.M. Gola, C. Badini, Modelling of TBC system failure: stress distribution as a function of TGO thickness and thermal expansion mismatch, Eng. Fail. Anal. 13 (2006) 409–426.
[14] P. Jiang, X. Fan, Y. Sun, D. Li, B. Li, T.J. Wang, Competition mechanism of interfacial cracks in thermal barrier coating system, Mater. Des. 132 (2017) 559–566.
[15] P. Jiang, X. Fan, Y. Sun, D. Li, T.J. Wang, Bending-driven failure mechanism and modelling of double-ceramic-layer thermal barrier coating system, Int. J. Solids Struct., 130- 131 (2018) 11–20.
[16] M. Peters, C. Leyens, U. Schulz, W.A. Kaysser, EB-PVD thermal barrier coatings for Aeroengines and gas turbines, Adv. Eng. Mater. 3 (2010) 193–204.
[17] L. Wang, L. Guo, Z. Li, H. Peng, Y. Ma, S. Gong, H. Guo, Protectiveness of Pt and $Gd_2Zr_2O_7$ layers on EB-PVD YSZ thermal barrier coatings against calcium–magnesium–alumina–silicate (CMAS) attack, Ceram. Int. 41 (2015) 11662–11669.
[18] J.L. Smialek, F.A. Archer, R.G. Garlick, The chemistry of Saudi Arabian sand - A deposition problem on helicopter turbine airfoils, in: Proceedings of the 24th International SAMPE Technical Conference 24th International SAMPE Technical Conference, 1992.
[19] J.L. Smialek, F.A. Archer, R.G. Garlick, Turbine airfoil degradation in the persian gulf war, JOM-US 46 (1994) 39–41.
[20] M.P. Borom, C.A. Johnson, L.A. Peluso, Role of environmental deposits and operating surface temperature in spallation of air plasma sprayed thermal barrier coatings, Surf. Coat. Tech., 86– 87 (1996) 116–126.
[21] J. Kim, M.G. Dunn, A.J. Baran, Deposition of volcanic materials in the hot sections of two gas turbine engines, J. Eeng. Gas. Turb. Power 115 (1992) V3T–V5T.
[22] F.H. Stott, D.J. De Wet, R. Taylor, The effects of molten silicate deposits on the stability of thermal barrier coatings for turbine applications at very high temperatures, in: Proceedings of the 24th International SAMPE Technical Conference 24th International SAMPE Technical Conference, 1992.
[23] S. Krämer, J. Yang, C.G. Levi, Infiltration-Inhibiting Reaction of Gadolinium Zirconate Thermal Barrier Coatings with CMAS Melts, J. AM. Ceram. Soc. 91 (2008) 576–583.
[24] S. Krämer, J. Yang, C.G. Levi, C.A. Johnson, Thermochemical interaction of thermal barrier coatings with molten CaO–MgO–Al2O3–SiO2 (CMAS) deposits, J. AM. Ceram. Soc. 89 (2006) 3167–3175.
[25] L. Li, D.R. Clarke, Effect of CMAS infiltration on radiative transport through an EB-PVD thermal barrier coating, Int. J. Appl. Ceram. Tech. 5 (2008) 278–288.
[26] C. Mercer, S. Faulhaber, A.G. Evans, R. Darolia, A delamination mechanism for thermal barrier coatings subject to calcium–magnesium–alumino-silicate (CMAS) infiltration, ACTA Mater. 53 (2005) 1029–1039.
[27] X. Chen, Calcium–magnesium–alumina–silicate (CMAS) delamination mechanisms in EB-PVD thermal barrier coatings, Surf. Coat. Tech. 200 (2006) 3418–3427.
[28] S. Krämer, S. Faulhaber, M. Chambers, D.R. Clarke, C.G. Levi, J.W. Hutchinson, A.G. Evans, Mechanisms of cracking and delamination within thick thermal barrier systems in aero-engines subject to calcium-magnesium-alumino-silicate (CMAS) penetration, Mater. Sci. Eng.: A 490 (2008) 26–35.
[29] T. Steinke, D. Sebold, D.E. Mack, R.V. En, D.S. Ver, A novel test approach for plasma-sprayed coatings tested simultaneously under CMAS and thermal gradient cycling conditions, Surf. Coat. Tech. 205 (2010) 2287–2295.
[30] X. Fan, R. Xu, T.J. Wang, Interfacial delamination of double-ceramic-layer thermal barrier coating system, Ceram. Int. 40 (2014) 13793–13802.
[31] R. Xu, X.L. Fan, W.X. Zhang, Y. Song, T.J. Wang, Effects of geometrical and material parameters of top and bond coats on the interfacial fracture in thermal barrier coating system, Mater. Des. 47 (2013) 566–574.
[32] X.L. Fan, R. Xu, W.X. Zhang, T.J. Wang, Effect of periodic surface cracks on the interfacial fracture of thermal barrier coating system, Appl. Surf. Sci. 258 (2012) 9816–9823.
[33] A.F. Renteria, B. Saruhan, U. Schulz, H.J. Raetzer-Scheibe, J. Haug, Effect of morphology on thermal conductivity of EB-PVD PYSZ TBCs, Surf. Coat. Tech. 201 (2006) 2611–2620.
[34] L.C. Su, X. Chen, T.J. Wang, Numerical analysis of CMAS penetration induced interfacial delamination of transversely isotropic ceramic coat in thermal barrier coating system, Surf. Coat. Tech. 280 (2015) 100–109.
[35] A.G. Evans, J.W. Hutchinson, The mechanics of coating delamination in thermal gradients, Surf. Coat. Tech. 201 (2007) 7905–7916.
[36] S. Sundaram, D.M. Lipkin, C.A. Johnson, J.W. Hutchinson, The Influence of Transient thermal gradients and substrate constraint on delamination of thermal barrier coatings, J. Appl. Mech. 80 (2013) 1002.
[37] R.W. Jackson, M.R. Begley, Critical cooling rates to avoid transient-driven cracking in thermal barrier coating (TBC) systems, Int. J. Solids Struct. 51 (2014) 1364–1374.
[38] X. Chen, J.W. Hutchinson, A.G. Evans, Simulation of the high temperature impression of thermal barrier coatings with columnar microstructure, ACTA Mater. 52 (2004) 565–571.
[39] X. Chen, R. Wang, N. Yao, A.G. Evans, J.W. Hutchinson, R.W. Bruce, Foreign object damage in a thermal barrier system: mechanisms and simulations, Mater. Sci. ENG.: A 352 (2003) 221–231.
[40] X. Chen, M.Y. He, I. Spitsberg, N.A. Fleck, J.W. Hutchinson, Mechanisms governing the high temperature erosion of thermal barrier coatings, Wear 256 (2004) 735–746.
[41] D.S.M.S, Corporation, ABAQUS User's Manual, 2009.
[42] B. Li, X. Fan, K. Zhou, T.J. Wang, Effect of oxide growth on the stress development in double-ceramic-layer thermal barrier coatings, Ceram. Int. 43 (2017)

14763–14774.
[43] R.W. Jackson, E.M. Zaleski, D.L. Poerschke, B.T. Hazel, M.R. Begley, Interaction of molten silicates with thermal barrier coatings under temperature gradients, ACTA Mater. 89 (2015).
[44] M. Ranjbar-Far, J. Absi, G. Mariaux, F. Dubois, Simulation of the effect of material properties and interface roughness on the stress distribution in thermal barrier coatings using finite element method, Mater. Des. 31 (2010) 772–781.
[45] M. Ranjbar-Far, J. Absi, S. Shahidi, G. Mariaux, Impact of the non-homogenous temperature distribution and the coatings process modeling on the thermal barrier coatings system, Mater. Des. 32 (2011) 728–735.
[46] T.R. Kakuda, C.G. Levi, T.D. Bennett, The thermal behavior of CMAS-infiltrated thermal barrier coatings, Surf. Coat. Tech. 272 (2015) 350–356.
[47] N.P.B. Valerie, L. Wiesner, Mechanical and thermal properties of calcium–magnesium aluminosilicate (CMAS) glass, J. Eur. Ceram. Soc. 35 (2015) 2907–2914.